

Published in final edited form as:

*IEEE Trans Med Imaging*. 2012 May ; 31(5): 1076–1085. doi:10.1109/TMI.2012.2185247.

## Projection X-Space Magnetic Particle Imaging

**Patrick W. Goodwill,**

Department of Bioengineering, University of California, Berkeley, CA 94720 USA.

**Justin J. Konkle,**

Department of Bioengineering, University of California, Berkeley, CA 94720 USA.

**Bo Zheng, Emine U. Saritas, and**

Department of Bioengineering, University of California, Berkeley, CA 94720 USA.

**Steven M. Conolly**

Department of Bioengineering, University of California, Berkeley, CA 94720 USA.

Patrick W. Goodwill: goodwill@berkeley.edu

### Abstract

Projection magnetic particle imaging (MPI) can improve imaging speed by over 100-fold over traditional 3-D MPI. In this work, we derive the 2-D x-space signal equation, 2-D image equation, and introduce the concept of signal fading and resolution loss for a projection MPI imager. We then describe the design and construction of an x-space projection MPI scanner with a field gradient of 2.35 T/m across a 10 cm magnet free bore. The system has an expected resolution of  $3.5 \times 8.0$  mm using Resovist tracer, and an experimental resolution of  $3.8 \times 8.4$  mm resolution. The system images  $2.5 \text{ cm} \times 5.0 \text{ cm}$  partial field-of views (FOVs) at 10 frames/s, and acquires a full field-of-view of  $10 \text{ cm} \times 5.0 \text{ cm}$  in 4 s. We conclude by imaging a resolution phantom, a complex “Cal” phantom, mice injected with Resovist tracer, and experimentally confirm the theoretically predicted x-space spatial resolution.

### Index Terms

Angiography biomedical imaging; magnetic particle imaging (MPI); magnetic particles

### I. Introduction

Magnetic particle imaging (MPI) is a new medical imaging modality with great promise for high-contrast angiography, cancer imaging, *in vivo* cell tracking, and inflammation imaging in humans and small animals.

First published in 2005 [1], the MPI technique has progressed rapidly. Recent hardware developments include: real-time MPI in a mouse [2]–[4], methods for single-sided MPI

using strongly nonlinear magnetic field gradients [5], and narrowband and x-space images of mice and phantoms [6]–[8].

Current state-of-the-art MPI is intrinsically 3-D due to the design of the main magnet [3], [8]. These main magnet designs form a single point in three-dimensions termed the field free point (FFP), where the magnetic field magnitude is weaker than the saturation magnetization of a magnetic nanoparticle tracer. An image is formed using a FFP by performing a voxel-wise scan of a 3-D volume. To date, all experimental MPI scans have been performed with a FFP.

Due to the extraordinary contrast and penetration of the MPI imaging modality, there are many applications for which a 2-D *projection* MPI image would be highly desirable. This is because only two dimensions need be scanned rather than three, and so projection scanning is inherently faster by a factor equal to the number of pixels in the projection direction. Hence, projection MPI is about *two orders of magnitude faster* than 3-D MPI. This increased speed will be critical for real-time angiography, stem cell imaging, and cancer detection using dynamic contrast enhancement. Indeed, we believe that MPI's preferred mode of operation may be fast projection imaging, akin to projection and fluoroscopic X-ray.

Key to forming a projection image is a field free line (FFL) main magnet [9]. A FFL is similar to the field free point (FFP) used in 3-D MPI scanners, except the FFL has close to zero field magnitude within a line-like region as opposed to a point-like region. There are many techniques for generating a field free line, which is equivalent to the quadrupolar magnetic field used in linear accelerators since the 1950s [10]. The first work to propose a FFL MPI magnet used simulations to show that a rotating and shifting a FFL could increase the sensitivity of the MPI technique by an order of magnitude [9]. This work was followed by Knopp *et al.*, who simulated a series of improved main magnet designs capable of electronically rotating the FFL [11], [12]. In addition, Knopp *et al.* built and characterized using hall effect measurements a nonrotating FFL electromagnet design with a gradient strength of 0.1 T/m [13]. All the prior literature on FFL magnets [9], [11]–[13] proposes translating and rotating the FFL to produce a 3-D image with improved SNR; we instead propose that using a FFL for a *projection* scan enables new classes of real-time tracer studies and high sensitivity tracer imaging.

Here, we build the first permanent magnet FFL gradient for MPI and provide the first MPI images taken with a FFL. The design inspiration for the FFL magnet used in this paper is the standard quadrupole magnet used in linear accelerators, which we approximate by constructing a four-rung  $\sin(2\phi)$  magnet using NdFeB permanent magnets. The number of rungs is a tradeoff between field homogeneity and access. Because the projection direction of a  $\sin(2\phi)$  quadrupole magnet is axial, we require access through the side of the magnet structure to introduce an animal or phantom. A four-rung approximation to the  $\sin(2\phi)$  distribution offers a full 180° of open access. FFL movements are performed using high power electromagnets and mechanically using a robot. The design concept and completed magnet are shown in Fig. 1.

In this paper, we begin by deriving analytical expressions in x-space for the projection MPI signal, system point spread function, and magnet homogeneity requirements. We then design and build an x-space MPI projection scanner, which we use to measure the system's native point spread function, image a complex "Cal" phantom, and image a mouse injected with tracer.

## II. MPI FFL Theory

Three MPI techniques have been shown experimentally. The most published technique is *harmonic-space* MPI, which uses a *system matrix*. The *system matrix* is comprised of Fourier components of the temporal signal for every possible location of a point source [1], [2], [4], [14]–[17]. Reconstruction is achieved through regularization and matrix inversion techniques such as singular value decomposition or algebraic reconstruction. The second technique is a narrowband technique, which reconstructs harmonic images into a composite image using a modified Wiener deconvolution [6], [7]. The third technique, which we use in this paper, is x-space MPI [8], [18], [19].

X-space MPI is a new theoretical approach to MPI signal processing and reconstruction that enables acquisition of a *native* MPI image, and does not require a *system function*, harmonics, or pre-characterization of the nanoparticles or imager. We described the x-space technique in detail in our first two x-space papers [8], [18]. X-space offers several advantages over harmonic-space MPI matrix reconstructions. Specifically, x-space MPI reconstruction offers experimentally proven linearity and shift invariance (LSI), as well as real-time image reconstruction speed [8]. Importantly, x-space reconstruction makes no attempt to deconvolve the MPI signal to improve resolution over the resolution determined by the physics of the nanoparticles and field gradient, and thus avoids the significant noise gain of deconvolution (see the noise gain in [20]).

The x-space technique relies on three major hypotheses: 1) that magnetic nanoparticles adiabatically align with an applied magnetic field, 2) that the FFP location is unique, and 3) that the loss of low frequency information due to filtering the fundamental is recoverable. In this section, we extend x-space theory to work with projection MPI. We first describe the signal and image equations, which differ from the 3-D case [8].

### A. Projection X-space MPI Signal Equation

The x-space theory of projection MPI builds on our previous work on multidimensional MPI. In multidimensional MPI, we derived the signal and image equations by assuming the FFP has a unique position in three dimensions. Maxwell's equations in a source free region imposes physical constraints on the achievable magnetic fields; as described in [8] and [21] the achievable magnetic field gradient can be written as a parameterized gradient matrix  $\mathbf{G} \in \mathbb{R}^{3 \times 3}$  with diagonal symmetry and trace  $\text{tr}(\mathbf{G}) = 0$  times the spatial vector. Specifically the magnetic field as a function of position can be written

$$\mathbf{H}(\mathbf{x}) = \mathbf{G}\mathbf{x} = \begin{bmatrix} -\alpha G_{zz} & G_{xy} & G_{xz} \\ G_{xy} & (\alpha - 1)G_{zz} & G_{yz} \\ G_{xz} & G_{yz} & G_{zz} \end{bmatrix} \begin{bmatrix} x \\ y \\ z \end{bmatrix} \quad (1)$$

with one free design parameter  $\alpha \in (0,1)$ . Fortunately, a FFL gradient for projection MPI along the  $y$  direction can be constructed while obeying Maxwell's equations. Suppose we design the FFL magnet so that  $\alpha = 1$  (or  $\alpha = 0$ ) and so that the cross terms  $G_{xy}$ ,  $G_{xz}$ , and  $G_{yz}$  are zero. This describes a physically realizable field, since the matrix has zero trace and diagonal symmetry

$$\mathbf{G} = \begin{bmatrix} -G_{zz} & 0 & 0 \\ 0 & 0 & 0 \\ 0 & 0 & G_{zz} \end{bmatrix}.$$

For this important case, the location of the free point would be undefined as the gradient matrix is singular. Note that this describes a FFL along the  $y$  direction.

To enable  $x$ -space theory with this gradient matrix, we first define the concept of a FFL. We define the FFL as the line across which the magnetic field magnitude is zero, which we assume here is straight but could in fact be curved. For this case, we write the gradient matrix in a reduced, nonsingular form.

Let us now assume that the FFL is along the  $y$  axis. Then, the magnetic field can be written

$$\mathbf{H}(\mathbf{x}) = \mathbf{G}_2 \mathbf{x} = \begin{bmatrix} -G_{zz} & G_{xz} \\ G_{xz} & G_{zz} \end{bmatrix} \begin{bmatrix} x \\ z \end{bmatrix}.$$

We can now shift the center of the field-of-view (FOV) using homogeneous magnetic fields

$$\mathbf{H}_s(t) = \begin{bmatrix} H_x(t) \\ H_z(t) \end{bmatrix}$$

where  $H_x(t)$  and  $H_z(t)$  are time varying, homogeneous magnetic fields that point in the  $x$  and  $z$  instrument axes. Giving the gradient a convenient negative sign, the total magnetic field as a function of time can be written as

$$\mathbf{H}(t, \mathbf{x}) = \mathbf{H}_s(t) - \mathbf{G}_2 \mathbf{x}.$$

Solving for  $\mathbf{x}$ , we see that the instantaneous location of the FFL is moved by the application of homogeneous magnetic fields. The instantaneous FFL center is located at the 2-D position

$$\mathbf{x}_s(t) = \mathbf{G}_2^{-1} \mathbf{H}_s(t).$$

The inverse of  $\mathbf{G}_2$  is guaranteed to exist since the determinant of the gradient matrix  $\det(\mathbf{G}_2) = -(G_{xz}^2 + G_{zz}^2)$  is nonzero for all nontrivial FFL gradients. Physically, this means that there exists a unique FFL in the uniform region of homogeneous field  $\mathbf{H}_s(t)$  and linear region of gradient field  $\mathbf{H}(\mathbf{x})$ .

Provided that the static field gradient is linear, the FFL moves linearly with the addition of magnetic fields in the  $x$  and  $z$  axes. It is important that the magnetic fields  $H_x(t)$  and  $H_z(t)$  have good homogeneity. This is because the addition of any magnetic field along the field free line (perpendicular to both  $x$  and  $z$ ) will cause the magnetic field experienced by the sample to not pass through zero, and will lead to signal *fading* and *resolution loss* artifacts. These artifacts are discussed in detail below in Section II-B.

Our results from 3-D multidimensional MPI directly apply to projection MPI when we use the revised gradient matrix definition [8]. Substituting into the *generalized signal equation*, we find that the signal equation remains a convolution

$$s(t) = \mathbf{B}_1(\mathbf{x}) m \rho_2(\mathbf{x}) ** \frac{\|\dot{\mathbf{x}}_s\|}{H_{\text{sat}}} \mathbf{h}(\mathbf{x}) \hat{\mathbf{x}}_s \Big|_{\mathbf{x}=\mathbf{x}_s(t)} \quad (2)$$

where  $\mathbf{B}_1(\mathbf{x})$  [T/A] is the receive coil sensitivity matrix,  $m$  [A/m<sup>2</sup>] is the magnetic moment of a single nanoparticle,  $\rho_2(x)$  [particles/m<sup>2</sup>] is the magnetic nanoparticle density,  $H_{\text{sat}}$  [A/m] is the saturation field of the magnetic nanoparticle,  $\mathbf{h}(\mathbf{x})$  is the point spread function, and  $\dot{\mathbf{x}}_s$  [m/s] is the FFL velocity vector. However, this equation differs from the 3-D case. First, the convolution does not occur in three dimensions as before, but in the plane perpendicular to the FFL. Second, we do not convolve the point spread function with the nanoparticle density, but the *projection* of the nanoparticle density along the FFL,  $\rho_2(x, z)$ . We can express the projection of the nanoparticle density as an integral

$$\rho_2(x, z) = \int \rho(x, y, z) dy.$$

The resulting units of the nanoparticle projection density function has the units of particles/m<sup>2</sup>. The point spread function equation remains the same as in the general 3-D case

$$\mathbf{h}(\mathbf{x}) = \mathcal{L} \left[ \frac{\|\mathbf{G}_2 \mathbf{x}\|}{H_{\text{sat}}} \frac{\mathbf{G}_2 \mathbf{x}}{\|\mathbf{G}_2 \mathbf{x}\|} \left( \frac{\mathbf{G}_2 \mathbf{x}}{\|\mathbf{G}_2 \mathbf{x}\|} \right)^T \mathbf{G}_2 + \frac{\mathcal{L} \left[ \frac{\|\mathbf{G}_2 \mathbf{x}\|}{H_{\text{sat}}} \right]}{\|\mathbf{G}_2 \mathbf{x}\| / H_{\text{sat}}} \left( \mathbf{I} - \frac{\mathbf{G}_2 \mathbf{x}}{\|\mathbf{G}_2 \mathbf{x}\|} (\mathbf{G}_2 \mathbf{x} \|\mathbf{G}_2 \mathbf{x}\|)^T \right) \mathbf{G}_2 \right]$$

where  $\mathcal{L}$  denotes the Langevin function. The projection reduces the dimensionality of the matrix PSF so that  $\mathbf{h}(\mathbf{x}) \in \mathbf{R}^{2 \times 2}$ .

We reconstruct the projection MPI image by dividing the raw collinear signal by the instantaneous velocity in  $x$ -space followed by gridding of the signal to the instantaneous FFL location in 2-D space. As proven below, this *extremely fast* processing step obtains a 2-D convolution of the point spread function with the ideal projection of the nanoparticle density

$$\hat{\rho}_2(\mathbf{x}_s(t)) = s_{\parallel}(t) / \|\dot{\mathbf{x}}_s\| = \rho_2(\mathbf{x}) \cdot \hat{\mathbf{x}}_s \cdot \mathbf{h}(\mathbf{x}) \hat{\mathbf{x}}_s \Big|_{\mathbf{x}=\mathbf{x}_s(t)} \quad (3)$$

It is important to understand that this fast x-space image reconstruction does *not* deconvolve the PSF  $\mathbf{h}(\mathbf{x})$  from the reconstructed image. Standard deconvolution methods may be added after this final reconstruction step, but these will inevitably reduce the final image SNR.

## B. FFL Homogeneity Requirements

The uniformity of the FFL is vital for projection imaging. Nonideality of the FFL results in two signal effects: signal fading and resolution loss. For low levels of nonideality, we approximate the loss of signal in a simple fading approximation as the resolution loss is less noticeable. For larger levels of nonideality, the resolution of the system can drop significantly. Here we describe both effects.

**1) Fading**—Fig. 2 shows how the point spread function changes for a point source passing through a nonideal field free line away from the magnet isocenter. Because the FFL is nonideal, particles near the ends of the FFL never pass through a field region with zero magnetic field. This partial passage through the Langevin curve leads to signal dropout near the ends of the FFL. We have designed the Berkeley FFL main magnet so that there is minimal signal dropout (<5% fading) using Resovist (Bayer–Schering) tracer.

We can describe the nonideality of the FFL as a gradient along the direction of the FFL. In our magnet, the FFL and consequently the undesired gradient is along the y axis, [which is equivalent to  $\alpha < 1$  in (1)]. Assuming the field free line is along the y axis, the maximum undesired magnetic field at any position along the y axis can be written

$$H_y = G_y y = (\alpha - 1) G_{zz} y. \quad (4)$$

We now introduce the term signal *fading* to describe the loss of image intensity due to FFL inhomogeneity. Let us assume we are measuring a point source at some position along the y axis. Then, the peak signal of a point source scanned at some position along the y axis can be estimated using the Normal signal envelope. From [8], the normalized peak signal as a function of a static offset field is

$$F = 3 \left( \frac{\coth(H_y/H_{\text{sat}}) - H_{\text{sat}}/H_y}{H_y/H_{\text{sat}}} \right) \quad (5)$$

where  $F$  is the remaining signal (see Fig. 3). For example, if  $F = 0.9$ , this describes a 10% fading from ideal. Equation (5) predicts 2% fading for Resovist tracer used in the Berkeley projection scanner ( $H_{y,\text{max}} = 1.6 \text{ mT}/\mu_0$  at  $\pm 2 \text{ cm}$ , Resovist  $H_{\text{sat}} \approx 3.3 \text{ mT}/\mu_0$ ,  $F = 0.98$ ). Of course, any FFL magnet design will suffer from some degree of fading, and a moderate amount (say 10% fading) will very likely be well tolerated clinically, similar to (the much greater) fading of the MRI signal with distance from an RF surface coil.

**2) Resolution Loss**—Magnet inhomogeneity reduces system resolution because the nanoparticle no longer passes through the full Langevin curve (see Fig. 2). Unfortunately, the widening of the full-width at half-maximum (FWHM) is difficult to express in a closed form solution. We can instead calculate the increase in FWHM numerically using the full x-space theory, which we show graphically in Fig. 3.

For moderate amounts of fading up to  $H/H_{\text{sat}} = 2$  which corresponds to  $\approx 20\%$  fading and resolution loss, the FWHM widening is approximately equal to the fading. For example, if there is 10% fading, there is approximately 10% loss in resolution. As the FFL nonideality increases beyond 20% fading and resolution loss, resolution loss begins to accelerate when compared to the fading.

While the main magnet described in this paper has minimal resolution loss with Resovist SPIO tracer at the far extents of the FFL, as new nanoparticles for MPI are developed the resolution loss can become a stronger design criteria. For example, a theoretical  $d = 30$  nm SPIO nanoparticle ( $H_{\text{sat}} \approx 0.6 \text{ mT}/\mu_0$ ) in the Berkeley FFL scanner would have over 20% resolution loss at the edges of the FOV unless we shim the main gradient magnet.

### C. Two Order of Magnitude Speed Improvement

The clearest benefit to a projection scan is an increase in speed. For a 3-D image, the FFP must scan every voxel in the received image. The number of voxels in a typical medical imaging scan can be large ( $N = 128^3$ ), and so a 3-D scan can take a substantial amount of time when all human safety considerations (limits on  $dB/dt$  and SAR) as well as power supply considerations are enforced. Thus, reducing the number of dimensions in an image reduces the number of voxels, which results in a concomitant increase in imaging speed. This increase in speed could enable the application of MPI to varied applications. For example, projection MPI would be ideal for real-time angiography with speeds approaching X-ray fluoroscopy, since the FFL can be moved just as fast as a FFP in a 3-D scanner. For perspective, the FFL in the Berkeley projection scanner is moving at more than 1200 m/s rms. If we instead desire to increase SNR rather than speed, projection scanning enables multiple image averages without increasing scan time over a 3-D scan of the same area.

## III. Magnet Design and Construction

In this section, we describe the magnet design criteria and system construction. The overall design concept was to construct a side-access quadrupole magnet. To achieve the magnetic field gradients necessary for moderate resolution MPI we decided to use NdFeB permanent magnets with no field return.

### A. Magnet Design Criteria

**Gradient Strength**—The native resolution of MPI potentially improves cubically with the nanoparticle diameter and linearly with the gradient strength [8], [17], [18]. To reach a target resolution, we must tailor the gradient strength to the specific nanoparticle used as a tracer. Our previous work with a small-scale MPI imaging system with a 6 T/m gradient and Resovist tracer achieved 1.6 mm resolution [8], with the distribution of particle diameters in Resovist behaving experimentally equivalent to a  $d = 17$  nm nanoparticle. Thus, with

Resovist tracer and linear scaling of the resolution with the gradient strength, we would require a 9 T/m gradient to achieve millimeter resolution. Unfortunately, this gradient strength is challenging to achieve with water-cooled copper gradients. Indeed, it is even difficult to achieve this gradient strength with high-grade NdFeB magnets. Hence, we decided to build a 2.35 T/m gradient, which was the largest gradient strength we could build given our internal manufacturing capabilities and FOV requirements.

According to x-space theory, a gradient of 2.35 T/m has an expected resolution of  $3.5 \times 8.0$  mm when imaging Resovist tracer, which behaves like a nanoparticle with a lognormal magnetic core diameter distribution of  $d = 17 \pm 4$  nm [19]. This expected resolution is for sample excitation and signal reception in only one instrument axis (the  $z$  axis in this imager). The expected resolution could be improved to  $3.5 \times 3.5$  mm by sample excitation in two axes ( $z$  and  $x$  in this imager), which we have not yet implemented in order to limit system complexity.

We note that increasing the gradient strength improves the resolution of the system at the expense of longer scanning times. This is because maximum excitation strength (in mTpp) is limited by magnetostimulation and SAR heating of the patient [18]. Then, a strong gradient reduces the imaging speed two-fold since increasing the gradient strength necessarily reduces the mean FFL velocity as well as increases the number of voxels in each image.

**Field-of-View (FOV)**—The magnet FOV is defined by the bore opening available to the sample, the maximum we can shift the field free line using fast and slow FFL shifting magnets, and the limits of robot movements. We have chosen a free bore of 4 cm to match the strength of the FFL shifting amplifier in the  $x$  axis as well as to enable mouse imaging. The FOV down the bore is limited only by robot movement.

**FFL Shift Linearity**—As we shift the FFL, it is crucial that the FFL remain undistorted and homogeneous across the field of view. The homogeneity of the shift field is important in the FFL axis ( $y$  axis), as any field components along the FFL will cause signal fading, as discussed above. The circular bore simplifies this since the length of the FFL can shorten as it shifts from the center. Inhomogeneity in the shift axes ( $x$ ,  $z$  axes) also leads to distortion of the field free line. Since the nanoparticles used in our system have a mean core diameter  $<20$  nm, the homogeneity requirements during FFL shifting are not difficult to meet. For higher core diameter particles the design of the main FFL and slow shifting magnets could require shimming or a more complex FFL magnet.

## B. Scanner Construction

The completed magnet next to a diagrammatic representation of the orientation and location of the NdFeB magnets that produce the main field gradient is shown in Fig. 1.

**NdFeB Magnet Construction**—The physical structure was designed in CAD software (Solidworks, Dassault Systèmes Solidworks Corp, MA) and constructed by the Berkeley Electrical Engineering Machine shop. To prevent eddy currents, the major components that experience time varying magnetic fields are constructed of G10 fiberglass composite, which is strong, nonmagnetic, and nonconductive. The magnets were assembled with custom jigs

(see Fig. 4) to overcome the significant magnetic forces estimated to be  $>2500$  newtons between the twelve rectangular NdFeB magnets during construction. The NdFeB magnets are electrically and magnetically isolated from the transmit and receive coils by a 2-mm-thick copper eddy current shield machined from high conductivity oxygen-free copper.

**FFL Shift Magnets**—The slow FFL shifting magnets are commercially produced, off-the-shelf water-cooled electromagnets (GMW Magnet 5403, GMW, San Carlos, CA) driven by a current-controlled linear power amplifier (AE Techron 7780, AE Techron, Elkhart, IN). The electromagnets achieve  $\pm 60$  mT at the center of the imaging bore with a peak power of approximately 5 kW. This can electronically shift the FFL by up to  $\pm 2.5$  cm in  $x$  in less than 100 ms. Both the shift distance as well as speed could be increased with the use of a more powerful amplifier.

**Transmit/Recv Subsystems**—The transmit filter system is constructed using a voltage-controlled linear power amplifier (AE Techron LVC5050) connected to a third-order lowpass filter driving a resonant, water-cooled transmit coil tuned to 22 kHz. The transmit chain achieves a 60 mT<sub>pp</sub> excitation strength at a 3 kW continuous power level, for a pFOV of 2.5 cm in the  $z$  axis. The transmit and receive coil formers are printed using a rapid prototyping system ZPrinter 150 (Burlington, MA) and impregnated in epoxy. The receive coil is wound in a gradiometer-like configuration so that it shares minimal mutual flux with the transmit coil. The transmit and receive coils are easily changed as they are loosely inserted in the copper eddy current shield. The received signal is notch filtered at 22 kHz, preamplified (SR560, SRS, Sunnyvale, CA), high pass filtered (SRS SIM965), and amplified with a second stage (SRS SIM911) before digitization.

**Control Console**—A data acquisition and control card (NIDAQ-6259, National Instruments, Austin, TX) synchronously controls the resonant transmit coil, FFL slow movement magnet, mechanical stage translation, and data acquisition. Control, data analysis, and reconstruction are all completed in custom software (MATLAB, Mathworks, Natick, MA).

## IV. Methods

### Simulation

Design of the magnet configuration was completed using a surface current model [22]. The surface current model enables an accurate estimation of the magnetic fields produced by NdFeB magnets by modeling the field produced using an equivalent surface current. Since the magnetic permeability of NdFeB is near unity at  $\mu_r \approx 1.05$ , the surface current model yields better than one percent accurate results at positions inside the bore of the magnet. This enables modeling the gradient strength for arbitrary permanent magnet gradients simply and rapidly without finite element modeling.

### Magnet Characterization

Following construction, the magnet was characterized with axial and transverse Hall Effect Probes (Model 475, LakeShore Cryotronics, Westerville, OH) mounted into a custom probe

mount. The hall effect probes were stepped throughout the FOV to measure all three field components.

### Imaging Pulse Sequence

The pulse sequence used to image the phantoms is shown in Fig. 5. In the imaging sequence, a resonant transmit coil moves the FFL at 22 kHz across a  $\pm 1.25$  cm region in the  $z$  axis. Slow FFL shifting magnets enable slower movement of the FFL up to  $\pm 2.5$  cm in the  $x$  axis. This enables the acquisition of an independent partial field-of-view (pFOV) of  $2.5 \text{ cm} \times 5.0 \text{ cm}$  at 10 frames/s. The shift speed and distance in the  $x$  axis are limited by the voltage and current, respectively, of the driving amplifier. Increasing both would enable faster scanning as well as a larger FOV. We step the patient table continuously during the scan in the  $z$  axis to acquire a full FOV of arbitrary length.

### Reconstruction

Each pFOV region is reconstructed by dividing the received signal by the instantaneous velocity of the FFL, and gridding the resulting signal to the instantaneous position of the FFL [8], [18]. For a given pFOV, we grid a  $N_z \times N_x = 50 \times 100$  pixel image. The resulting pFOVs are reconstructed into a full FOV as described in our previous work [8] by recovering the lost fundamental signal, as detailed in the next paragraph.

All MPI scanning methods must filter out the fundamental tone (and any nanoparticle signal at the same frequency) since the received signal is contaminated by direct feedthrough from source to detector. Fortunately, it is possible to recover the imaging information lost in this operation, which translates directly to recovering each pFOV's dc offset. We recover this lost information by using continuity and by assuming zero signal outside the FOV [8].

### Mouse Imaging

Mice were prepared by injecting in a tail vein with  $20 \mu\text{L}$  undiluted Resovist tracer, followed by sacrifice after 30 s or sacrifice after 5 min. Mice were sacrificed by  $\text{CO}_2$  asphyxiation in a precharged chamber followed by cervical dislocation. Mice were prepared according to a mouse protocol approved by the ACUC at UC Berkeley.

## V. Results and Discussion

We characterized the magnet with two techniques. First, we measured the magnetic fields achieved by the main FFL magnet and compared them to the theoretically expected fields from the surface current model. Second, we characterized the imaging system for resolution, linearity, and ability to image complex phantoms in a projection format.

### A. Magnet Characterization

In Fig. 6 we see the gradient strength along each axis through the isocenter of the bore. The magnet axes can be seen labeled in Fig. 1, where  $y$  is vertical along the field free line,  $x$  is the horizontal imaging axis, and  $z$  is down the magnet bore. As expected, the gradient along the field free line is small and stays below 0.08 T/m across the 4 cm imaging FOV, which corresponds to  $\pm 1.6$  mT field error at the ends of the FFL. The actual system homogeneity

may be better than this value as we believe that the hall effect sensor rotational alignment dominates our measurement error. For Resovist, this level of homogeneity results in less than 5% fading.

In Fig. 7, we see the characterization of the main gradient compared to the magnetic field predicted by the surface current model. The field measurements agree with the surface current simulations to better than 1%.

## B. Imaging Results

In Fig. 8, we see a test of the resolution of the projection scanner. The measured resolution using Resovist tracer is 3.8 mm in  $z$  (down the bore), and 8.4 mm in  $x$  (transverse to the bore), which matches reasonably with the expected system resolution of  $3.5 \times 8.0$  mm.

Fig. 8 also tests the linear shift-invariance (LSI) properties of the projection scanner. The system is LSI only *after* the dc offset recovery algorithm [8] is applied. In medical imaging, LSI properties are not guaranteed. For example, X-ray computed tomography (CT) imaging is a canonical example of a useful imaging technique that is not, strictly speaking, LSI. However, making a system approximately LSI is *fundamental* to medical imaging. CT linearizes the X-ray signal by taking its logarithm. Ultrasound scales the returned signal by a function that is exponential with time. And in  $x$ -space MPI we must velocity correct our received signal and we must also recover the low frequency data in order to guarantee that our signal varies linearly with quantity and position of tracer throughout the full FOV.

In Fig. 9, we see a demonstration of the projection capabilities of the Berkeley FFL scanner. This image was taken by physically moving a point source along the projection axis  $y$ , as well as down the bore. The resulting image shows how the shape of the point spread function changes little as a function of position along the projection. As predicted by  $x$ -space fading theory, the signal does not fade near the edges of the FOV. In fact, the signal *increases* near the edges of the FOV due to a  $\mathbf{B}_1(\mathbf{x})$  receive coil inhomogeneity of approximately 20%, which we plan to fix in future revisions to the transmit and receive coils.

In Fig. 10, we see a photo of a complex MPI phantom as well as a projection MPI image of the phantom. As can be seen in the image, the  $x$ -space MPI technique results in native MPI images over large FOVs. Unlike *system function* reconstruction techniques [17],  $x$ -space image reconstruction requires no precharacterization of the imaging system and nanoparticle tracer. System function reconstruction hinges upon the assumption that nothing will change in the MPI signal between the calibration study (performed in saline) and the actual scan in more viscous blood. Indeed, it is well known that viscosity varies substantially between arterial and capillary system. This could be another challenge for the system matrix reconstruction. *System function* techniques are used by other MPI imaging groups including [1], [4], [15].

There are two primary artifacts in the native MPI image in Fig. 10(b): baseline recovery artifacts, and signal dropout artifacts. The baseline recovery artifact is due to noise and system drift in the received signal that result in incorrect baseline stitching. We can see this

baseline artifact between the “C” and the “a,” where baseline recovery has added a slight background ( $\approx 7\%$  of full scale) to the image. Further averaging ( $N = 2$  for this image) reduces baseline recovery artifacts. There is also a signal dropout artifact present at the top and bottom of the “C.” We believe the signal dropout occurs due to reduced image resolution in the transverse direction inherent to the collinear point spread function [8].

In Fig. 11, we see full-body MPI projection images of two mice injected in a tail vein with  $20 \mu\text{L}$  undiluted Resovist. Following a tail injection, one animal was sacrificed after 30 s, and the second after 5 min. The animals were imaged immediately in the Berkeley projection MPI scanner. The MPI images are lightly deconvolved with Wiener filtering [23] to visually clean up the background in the image due to the low resolution of the system. Later, the animals were scanned with a 3T Siemens MRI scanner. The MPI and MRI images were co-registered with MPI-MRI visible fiducials. The most striking feature of the MPI scans is their contrast, particularly when compared with the MRI images. The MPI technique produces *perfect* contrast, as tissue has no MPI signal. The image of a mouse sacrificed after 30 s shows clear perfusion of the tracer to the brain and heart, and limited tracer in the liver. After 5 min circulation, the dominant location of the tracer is in the liver, and lower tracer levels in the brain. In the MRI images, the SPIO tracer causes a nonspecific  $T_2^*$  dropout in the 30-s mouse and a full  $T_2^*$  dropout of the liver after 5 min. Since Resovist is a liver targeting agent for liver cancer diagnosis using MRI, the rapid filtering of the tracer by the liver is not surprising.

Fig. 8, 10, and 11 demonstrate the high contrast inherent to MPI. We believe this contrast is ideal for rapid angiography, which has the simple goal of obtaining a high contrast image of the blood vessels. The MPI technique may also find use in other techniques that aim to see a tracer with high contrast and sensitivity, such as dynamic contrast enhancement (DCE) detection of tumors or imaging of labeled stem cells. For these techniques it may be desirable to co-register an MPI image with a tissue image, and so MPI could be combined with a second imaging modality such as MRI or CT in a manner analogous to PET-CT or SPECT-CT (as demonstrated in Fig. 11).

The improvement in imaging speed when using a projection imager over a 3-D imager with the same gradient strength is limited by the native resolution of the system. For example, with the current system resolution of 3.8 mm, a projection across the 5 cm FOV results in a speedup of 26 times when assuming a  $2\times$  oversampling of 1.9 mm per pixel. While this speedup falls short of the two order of magnitude speed improvement for an ideal clinical FFL scanner, this system is just a starting point as we continue to develop new generations of projection MPI scanners. The current system already images pFOVs at 10 frames/s (FPS), which could be improved through the use of a more powerful amplifier or a resonant circuit. Imaging speed for the full FOV is presently limited by the mechanical translation of the sample in the  $z$  axis. Full FOV imaging time could be improved through the construction of an additional set of electromagnets to move the FFL over large distances in the  $z$  axis instead of using mechanical movement.

While we believe that the image quality is an advance in the state of the art, it is important to consider that the 3.8 mm resolution of the Berkeley FFL scanner when imaging Resovist

tracer pales when compared with state-of-the-art micro-CT and micro-MRI scanners. Typical resolution in these preclinical techniques are in the 100- $\mu\text{m}$  range or finer. Fortunately, there are a number of techniques we can use to increase the resolution of x-space MPI. First, deconvolution methods may be employed to improve MPI spatial resolution [1], [17], [20], but these risk significant deconvolution artifacts and noise amplification. Gains in resolution may also be achieved by increasing the gradient strength of the system at the expense of longer scan times and reduced SNR. For example, we have built two 6 T/m FFP main field gradients for 3-D imaging of that are large enough to image mice [7], [8]. Last, we believe spatial resolution may be less of a challenge in the future as nanoparticle research groups work to tailor magnetic nanoparticles for MPI [24]–[26]. Because the linear spatial resolution of MPI scales *cubically* with particle diameter, larger diameter nanoparticles offer extraordinary promise for improving spatial resolution. For example, by moving to 34-nm diameter nanoparticles and imaging at a 6 T/m field strength, we theoretically expect to improve spatial resolution 20-fold to 190  $\mu\text{m}$  spatial resolution. Of course, important experimental considerations must be tested with the larger nanoparticles, including increased relaxation effects and potential loss of super-paramagnetism.

## VI. Conclusion

In this paper, we have analytically described, designed, constructed, and tested a projection MPI imager. The system reconstructs using our recently developed x-space systems theory, which enabled reconstruction without precharacterization of the imaging tracer, harmonics, or matrix inversion techniques. X-space MPI further ensures that the resulting image is Linear and Space-invariant, which is apparent when imaging a complex “*Cal*” phantom.

We believe this paper is the first to present experimental projection MPI images in phantoms as well as in mice. Moreover, we believe the image of the “*Cal*” phantom is an advance to the state of the art, both in image quality and the large field of view. These results are encouraging as we develop sub-millimeter (native resolution) x-space MPI systems, as well as wider-bore x-space MPI scanners.

Projection MPI is a promising new imaging format for MPI that could improve imaging speed by two orders of magnitude with no loss of SNR. The improvement in speed would be useful in real-time applications such as MPI “*fluoroscopy*,” dynamic contrast enhancement, and interventional MPI. MPI “*fluoroscopy*” holds particular promise as a safe rapid angiography technique because the safety profile of SPIO nanoparticle tracers [27], [28]. Alternatively, we could improve 2-D SNR by an order of magnitude over 3-D MPI by using the faster acquisition rate to increase averaging time. This mode of acquisition would be particularly well suited for cell tracking with labeled SPIO reporters where sensitivity is paramount.

## Acknowledgments

The authors would like to thank W. Yang and O. Carrasco-Zevallos for their excellent assistance.

This work was supported in part by CIRM Tools and Technology Grant RT1-01055-1, and a UC Discovery grant. The contents of this publication are solely the responsibility of the authors and do not necessarily represent the official views of CIRM or any other agency of the State of California. This work was supported in part by the

National Institute of Biomedical Imaging and Bioengineering under Grant 1R01EB013689. . The content is solely the responsibility of the authors and does not necessarily represent the official views of the National Institute of Biomedical Imaging and Bioengineering or the National Institutes of Health.

## References

1. Gleich B, Weizenecker J. Tomographic imaging using the nonlinear response of magnetic particles. *Nature*. 2005 Jun.435(no. 7046):1214–1217. [PubMed: 15988521]
2. Gleich B, Weizenecker J, Borgert J. Experimental results on fast 2-D-encoded magnetic particle imaging. *Phys. Med. Biol.* 2008 Feb.53:N81–N84. [PubMed: 18367783]
3. Weizenecker J, Gleich B, Rahmer J, Dahnke H, Borgert J. Three-dimensional real-time in vivo magnetic particle imaging. *Phys. Med. Biol.* 2009 Feb.54(no. 5):L1–L10. [PubMed: 19204385]
4. Weizenecker J, Borgert J, Gleich B. A simulation study on the resolution and sensitivity of magnetic particle imaging. *Phys. Med. Biol.* 2007 Nov.52(no. 21):6363–6374. [PubMed: 17951848]
5. Sattel TF, Knopp T, Biederer S, Gleich B, Weizenecker J, Borgert J, Buzug TM. Single-sided device for magnetic particle imaging. *J. Phys. D: Appl. Phys.* 2008 Dec.42(no. 2) 022001.
6. Goodwill P, Scott G, Stang P, Conolly S. Narrowband magnetic particle imaging. *IEEE Trans. Med. Imag.* 2009 Aug.28(no. 8):1231–1237.
7. Goodwill P, Conolly S. Narrowband magnetic particle imaging in a mouse. *World Scientific: Proc. 1st Int. Workshop Magn. Particle Imag.* 2010
8. Goodwill P, Conolly S. Multi-dimensional x-space magnetic particle imaging. *IEEE Trans. Med. Imag.* 2011 Sep.30(no. 9):1581–1590.
9. Weizenecker J, Gleich B, Borgert J. Magnetic particle imaging using a field free line. *J. Phys. D: Appl. Phys.* 2008 May.41(no. 10):105009.
10. Courant ED, Livingston MS, Snyder HS. The strong-focusing synchrotron—A new high energy accelerator. *Phys. Rev.* 1952; 88(no. 5):1190–1196.
11. Knopp T, Erbe M, Biederer S, Sattel TF, Buzug TM. Efficient generation of a magnetic field-free line. *Med. Phys.* 2010; 37(no. 7):3538. [PubMed: 20831060]
12. Knopp T, Sattel T, Biederer S. Field-free line formation in a magnetic field. *J. Phys. A: Math. Theor.* 2010
13. Knopp T, Erbe M, Sattel TF, Biederer S, Buzug TM. Generation of a static magnetic field-free line using two Maxwell coil pairs. *Appl. Phys. Lett.* 2010; 97(no. 9) 092505.
14. Knopp T, Biederer S, Sattel T, Weizenecker J, Gleich B, Borgert J, Buzug TM. Trajectory analysis for magnetic particle imaging. *Phys. Med. Biol.* 2008 Dec.54(no. 2):385–397. [PubMed: 19098358]
15. Knopp T, Sattel TF, Biederer S, Rahmer J, Weizenecker J, Gleich B, Borgert J, Buzug TM. Model-based reconstruction for magnetic particle imaging. *IEEE Trans. Med. Imag.* 2010 Jan.29(no. 1): 12–18.
16. Knopp T, Biederer S, Sattel T, Rahmer J, Weizenecker J, Gleich B, Borgert J, Buzug T. 2-D model-based reconstruction for magnetic particle imaging. *Med. Phys.* 2010; 37:485. [PubMed: 20229857]
17. Rahmer J, Weizenecker J, Gleich B, Borgert J. Signal encoding in magnetic particle imaging: Properties of the system function. *BMC Med. Imag.* 2009; 9(no. 1):4.
18. Goodwill PW, Conolly SM. The x-space formulation of the magnetic particle imaging process-1-D signal, resolution, bandwidth, SNR, SAR, and magnetostimulation. *IEEE Trans. Med. Imag.* 2010 Nov.29(no. 11):1851.
19. Goodwill P, Tamrazian A, Croft L, Lu C, Johnson E, Pidaparathi R, Ferguson R, Khandhar A, Krishnan K, Conolly S. Ferrohydrodynamic relaxometry for magnetic particle imaging. *Appl. Phys. Lett.* 2011; 98
20. Knopp T, Biederer S, Sattel TF, Erbe M, Buzug TM. Prediction of the spatial resolution of magnetic particle imaging using the modulation transfer function of the imaging process. *IEEE Trans. Med. Imag.* 2011 Jun.30(no. 6):1284–1292.

21. Bernstein M, Zhou X, Polzin J, King K, Ganin A, Pelc N, Glover G. Concomitant gradient terms in phase contrast MR: Analysis and correction. *Magn. Reson. Med.* 1998; 39:300–308. [PubMed: 9469714]
22. Furlani, EP. *Permanent Magnet and Electromechanical Devices: Materials, Analysis, and Applications.* New York: Elsevier; 2001.
23. Gonzalez, RC.; Woods, R Eugene. *Digital Image Processing.* Upper Saddle Rive, NJ: Prentice Hall; 2008.
24. Ferguson RM, Minard KR, Krishnan KM. Optimization of nanoparticle core size for magnetic particle imaging. *J. Magn. Magn. Mater.* 2009; 321(no. 10):1548–1551. [PubMed: 19606261]
25. Krishnan KM. Biomedical nanomagnetism: A spin through possibilities in imaging, diagnostics, and therapy. *IEEE Trans. Magn.* 2010 Jul.46(no. 7):2523–2558. [PubMed: 20930943]
26. Ferguson RM, Minard KR, Kandhar AP, Krishnan KM. Optimizing magnetite nanoparticles for mass sensitivity in magnetic particle imaging. *Med. Phys.* 2011 Mar.38(no. 3):1619–1626. [PubMed: 21520874]
27. Neuwelt E, Hamilton B, Varallyay C, Rooney W, Edelman R, Jacobs P, Watnick S. Ultrasmall superparamagnetic iron oxides (US-PIOs): A future alternative magnetic resonance (MR) contrast agent for patients at risk for nephrogenic systemic fibrosis (NSF)? *Kidney Int.* 2009; 75(no. 5): 465. [PubMed: 18843256]
28. Lu M, Cohen MH, Rieves D, Pazdur R. FDA report: Ferumoxytol for intravenous iron therapy in adult patients with chronic kidney disease. *Am. J. Hematol.* 2010 May; 85(no. 5):315–319. [PubMed: 20201089]

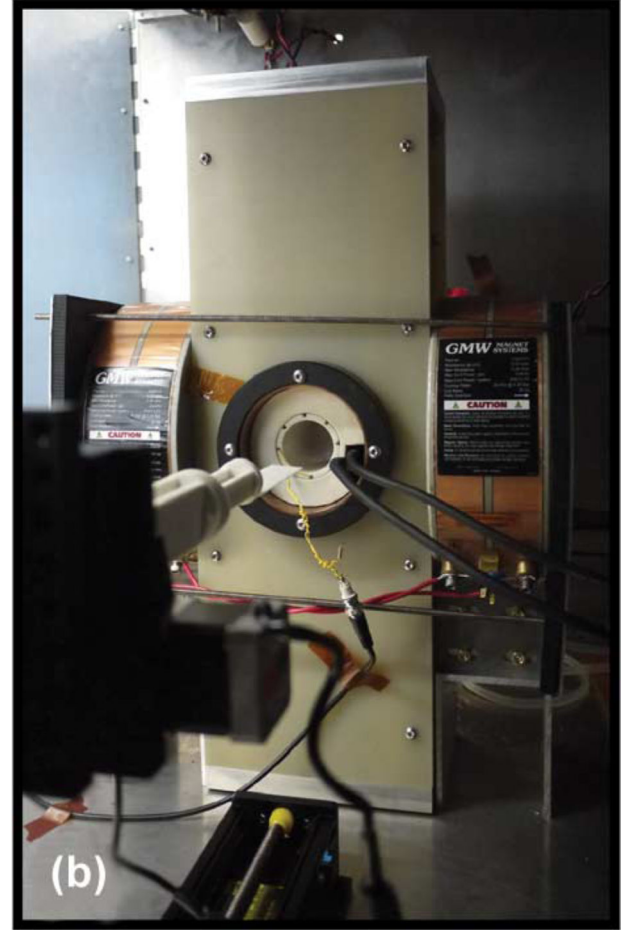
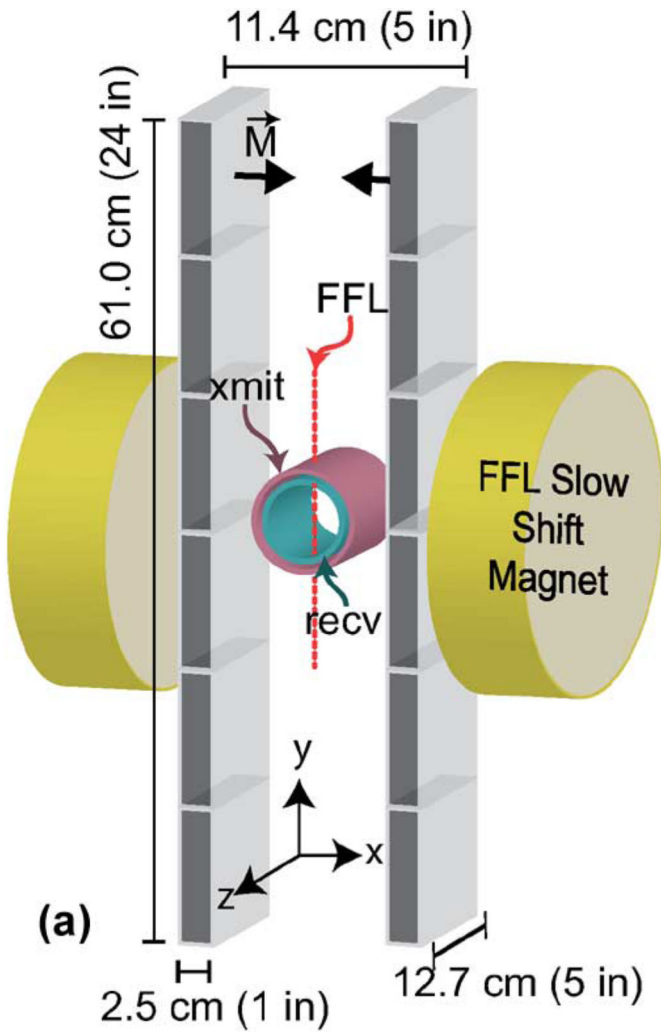


**Fig. 1.** First projection MPI scanner based on a quadrupole magnet built using NdFeB magnets. (a) Diagram showing all the magnets in the Berkeley FFL scanner. The NdFeB magnets are mounted in a G10 fiberglass composite and aluminum frame, which generates a FFL collinear to the  $y$  axis (dotted red line). NdFeB magnet magnetization orientation is shown with arrows. The FFL slow shift electromagnets enable shifting the FFL along the  $x$  axis. The resonant xmit coil shifts the FFL rapidly along the  $z$  axis. The recv coil receives the nanoparticle signal. (b) Completed projection MPI scanner.

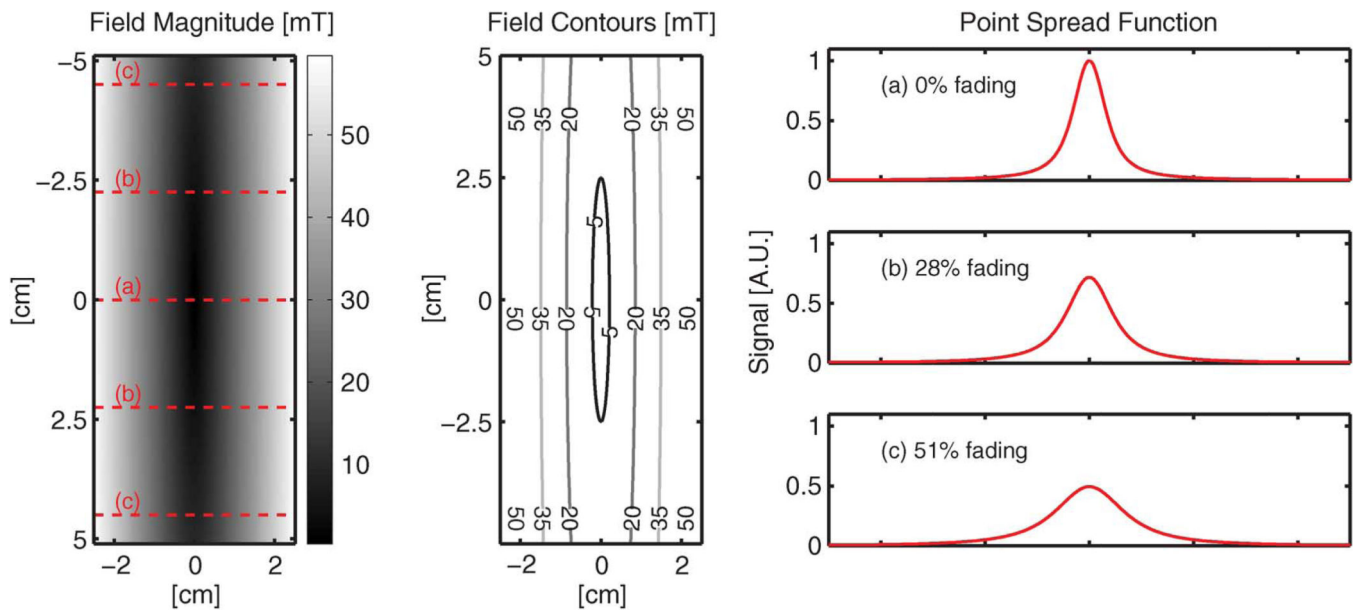


**Fig. 2.** Nonideality in a FFL causes signal loss and widening of the PSF. We can approximate small FFL nonidealities as a reduction in signal amplitude, or signal *fading*. The Berkeley magnet achieves <5% fading.

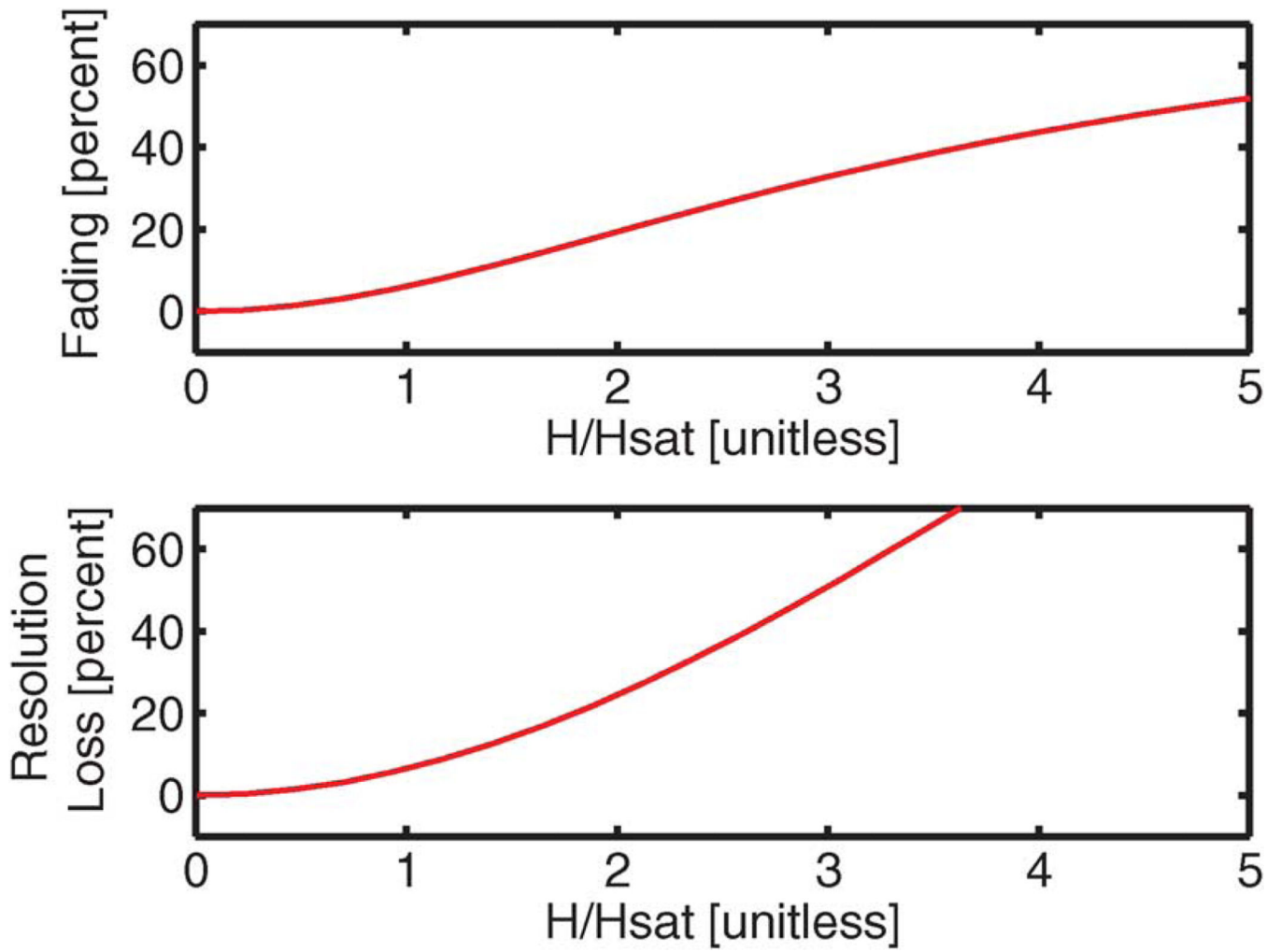
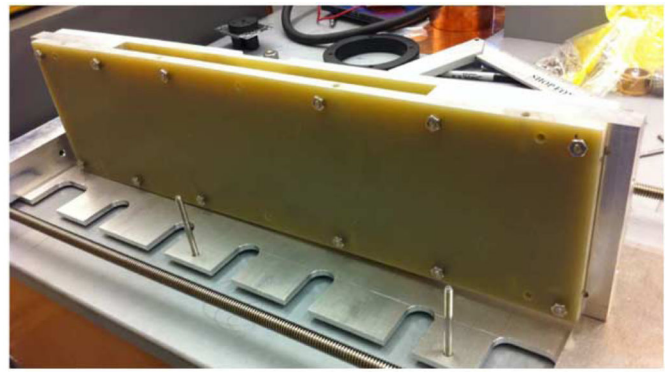


**Fig. 3.** Increasing levels of FFL inhomogeneity worsen fading and resolution. For FFL inhomogeneity values of  $H/H_{\text{sat}} < 2$ , resolution loss and fading are approximately equal in magnitude.



(a)



(b)

**Fig. 4.**

Main magnet is constructed in two halves using custom assembly jigs. The forces between the six NdFeB main magnet pieces during assembly are estimated at  $>2500$  newtons. (a) Jig to assemble the six NdFeB magnets rectangles into a main magnet. (b) Completed main magnet half.

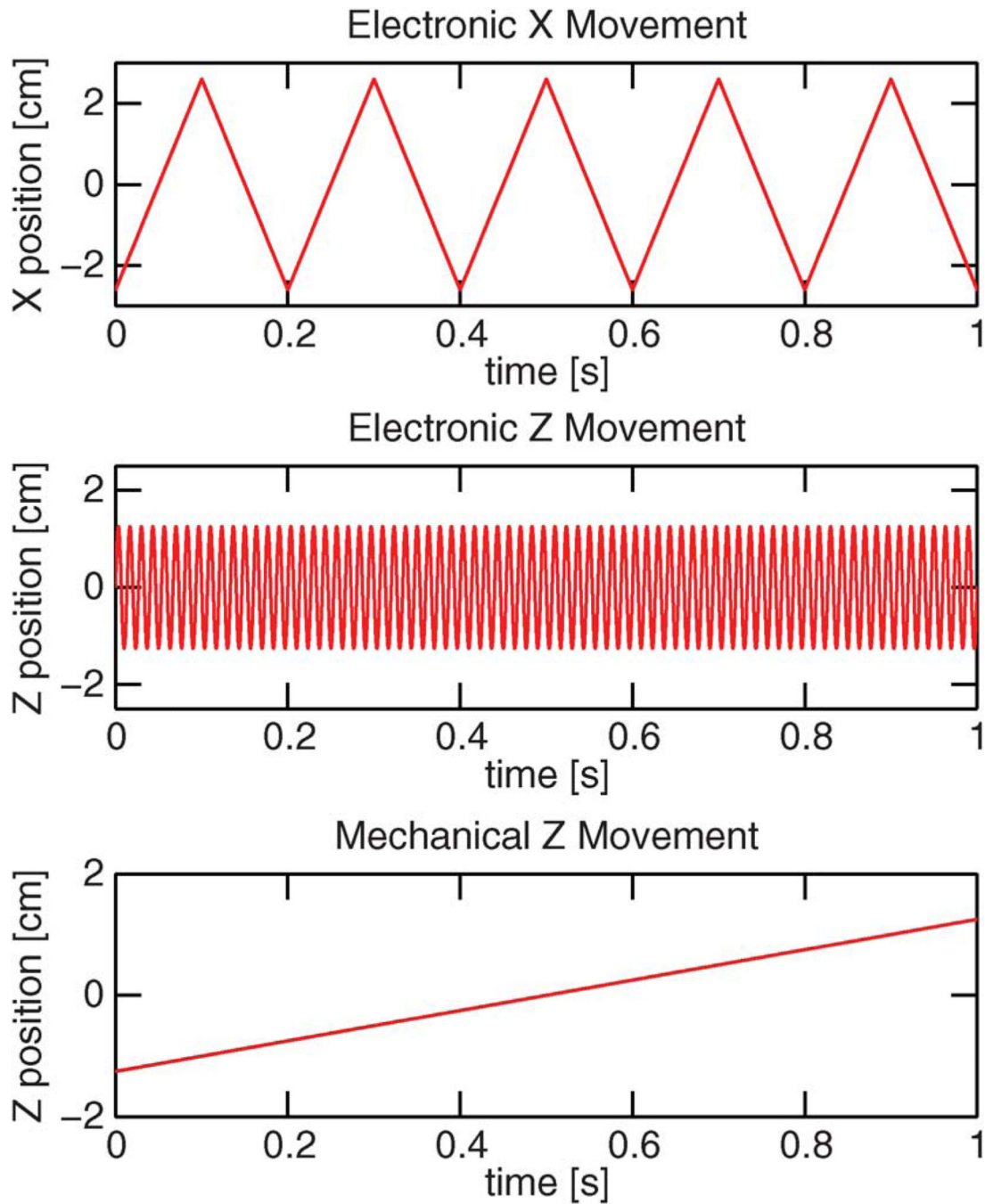


**Fig. 5.**

10 FPS pFOV pulse sequence: A representative portion of the pulse sequence used in the Berkeley Projection MPI scanner designed to observe dB/dt limits in a mouse while achieving fast partial FOV frame rates. The pulse sequence enables scanning a partial FOV of 2.5 cm  $\times$  5.0 cm at 10 frames/s. [Top] Movement in the  $x$  axis is performed using a pair of water cooled solenoids that shift up to  $\pm 2.5$  cm in approximately 100 ms. [Middle] Rapid sinusoidal movement at 22 kHz occurs in the  $z$  axis using a resonant, water cooled

electromagnet that shifts up to  $\pm 1.25$  cm. [Bottom] The sample is translated at 2.5 cm/s in the  $z$  axis using a mechanical stage to enable scanning the full FOV.

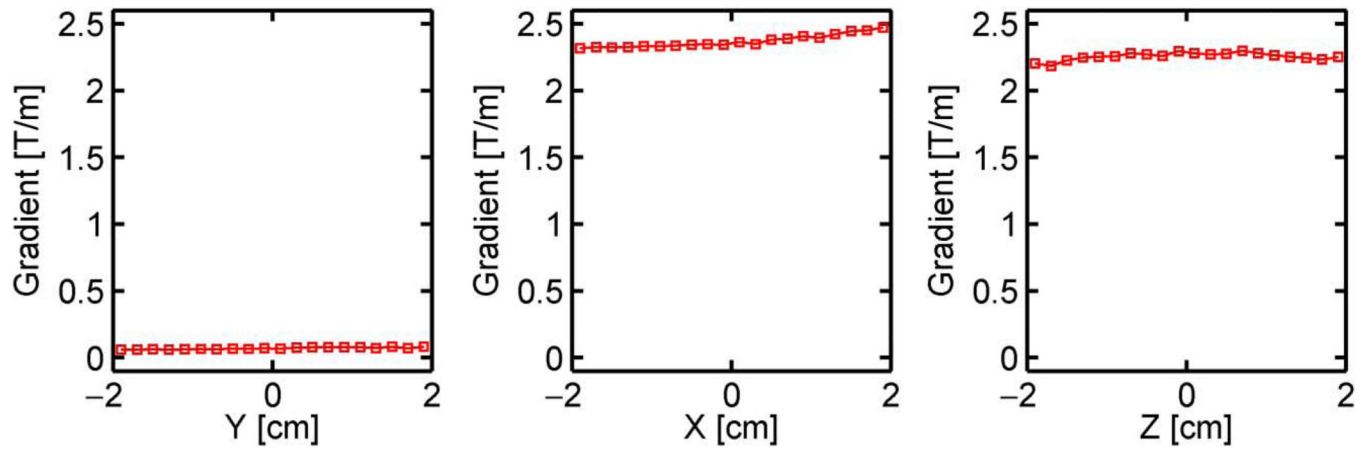


**Fig. 6.**

Field gradient in the principal axes of the completed FFL magnet, measured using a hall effect probe and numerical differentiation. The system achieves a 2.35 T/m gradient strength in  $x$  and  $z$ , and less than 0.08 T/m in  $y$ . Across a 4-cm FOV, this amounts to a undesired magnetic field component of only  $\pm 1.6$  mT at the edges of the FOV.

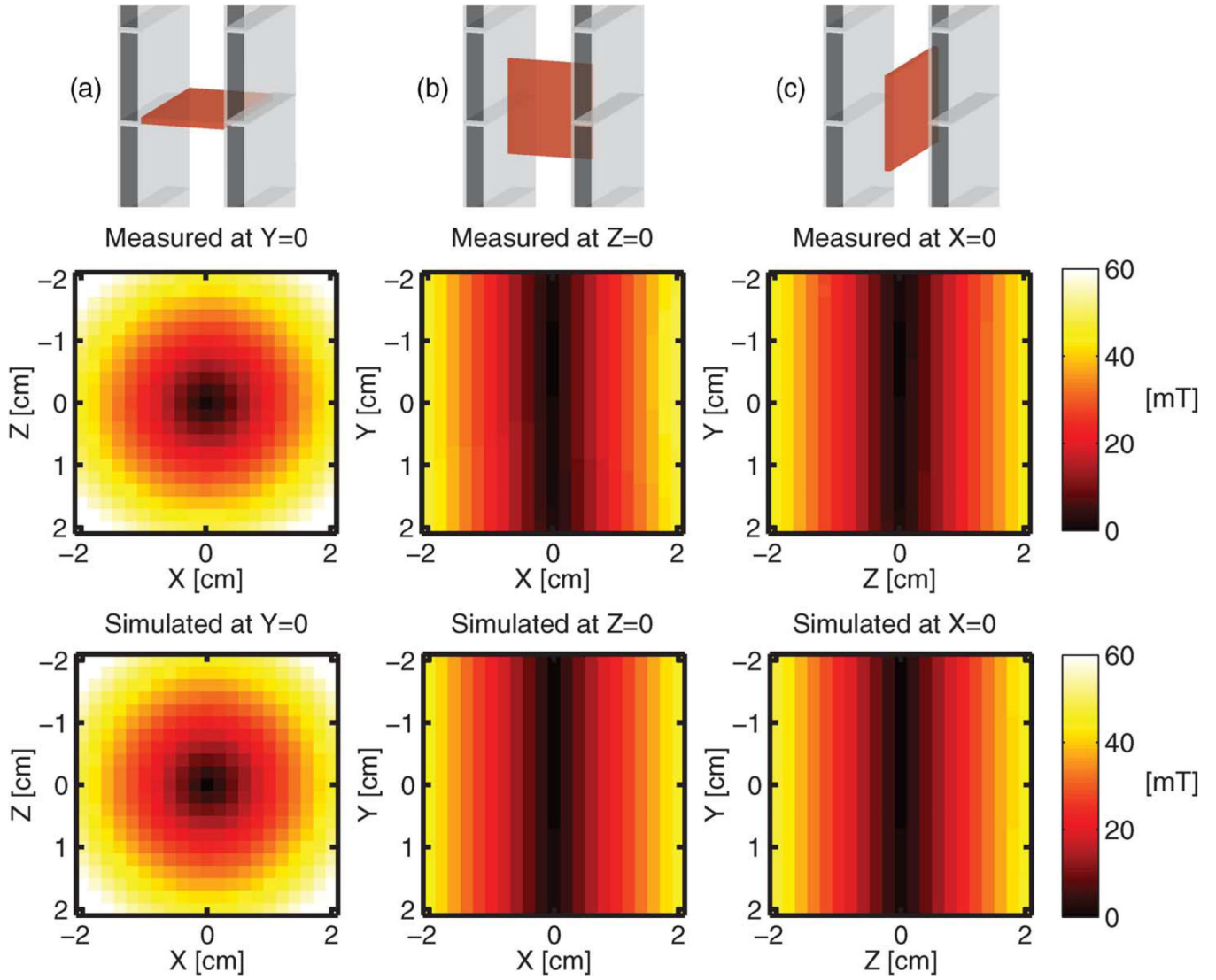
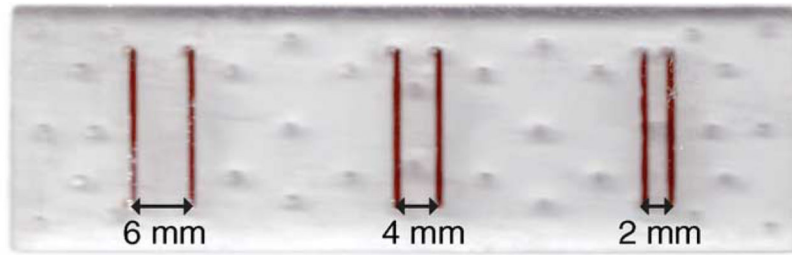
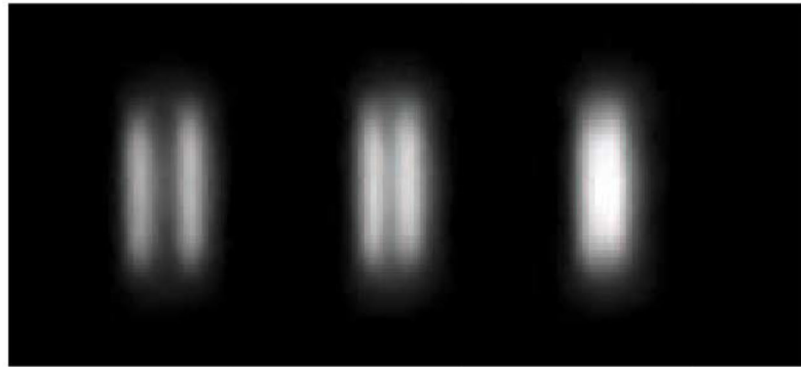


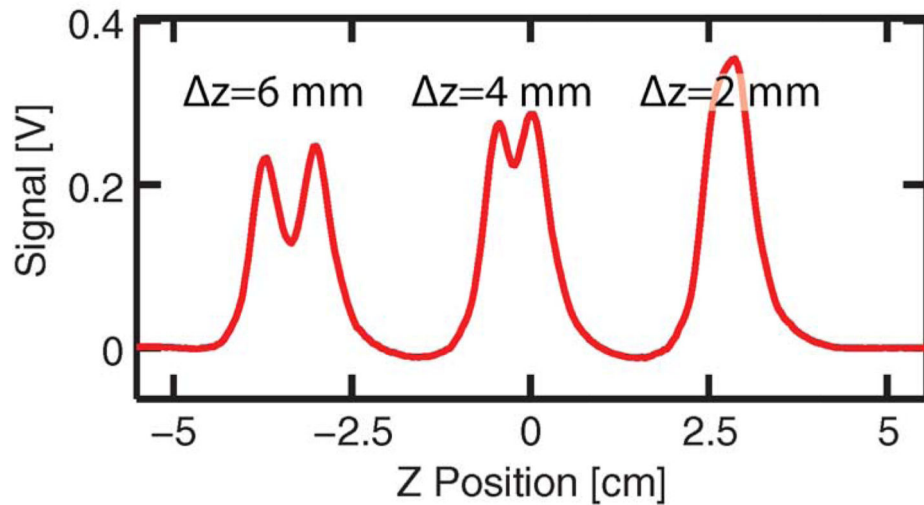
**Fig. 7.** Comparison of the Hall effect field measurements and the Biot–Savart simulation of the FFL magnet. The surface current model adequately models the NdFeB magnets to better than 1%.



(a)



(b)



(c)

**Fig. 8.**

Experimental resolution test of line sources separated below, above, and strongly above the native resolution of the system. (a) The phantom was constructed using laser cut channels filled with diluted tracer (one part Resovist, nine parts DI water). (b) Native x-space MPI image with total acquisition time of 4 s. FOV: 10 cm  $\times$  5.0 cm. (c) Line scan across position  $x = 0$ . The measured resolution is 3.8 mm in the z axis (down the bore), and 8.4 mm in the x axis (transverse to the bore). The experimental resolution reasonably matches the expected system resolution of  $3.5 \times 8$  mm.

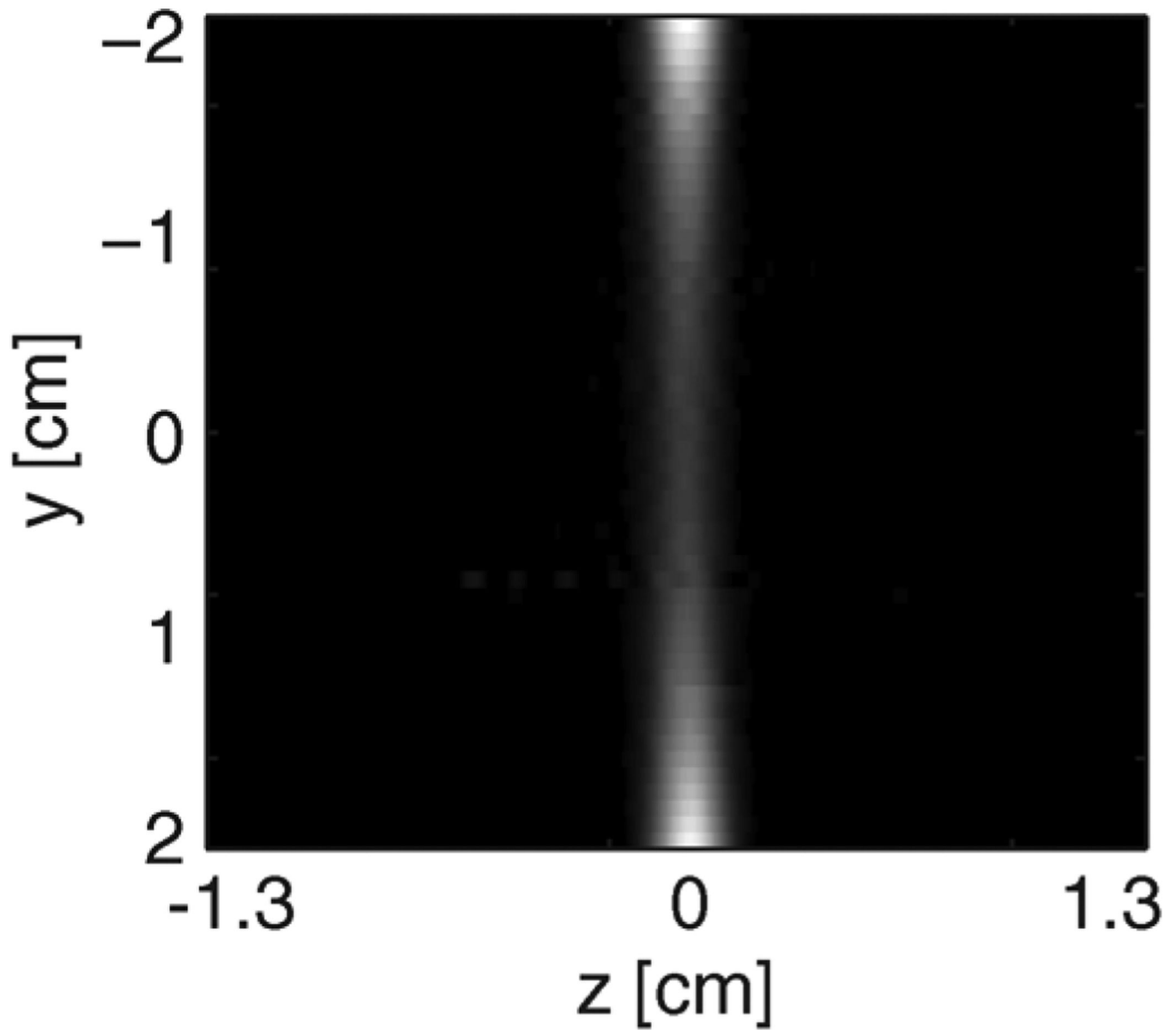
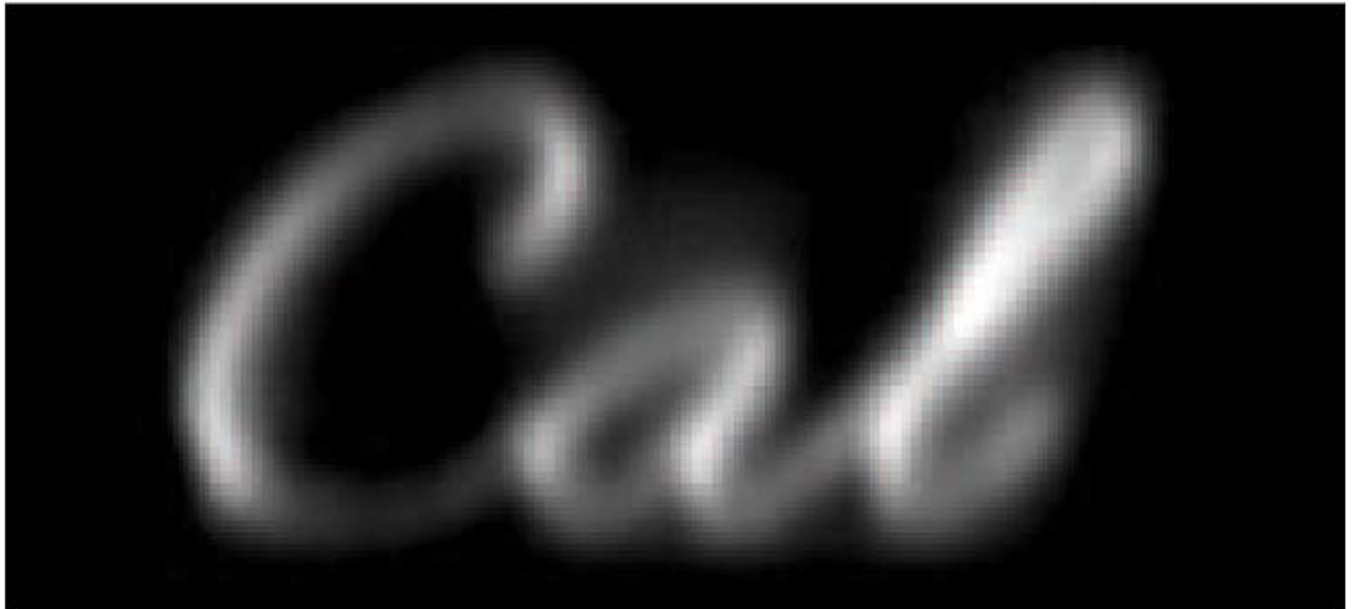


**Fig. 9.** Image of a point source physically rastered in the  $y$  axis (vertical projection axis) and  $z$  axis (down the bore). The signal increases at the ends of the line because the  $B_1$  receive coil sensitivity is not perfectly homogeneous.



(a)



(b)

**Fig. 10.**

Projection MPI image of a complex *Cal* phantom. (a) The physical “*Cal*” phantom is filled with diluted Resovist (one part Resovist, nine parts DI water). (b) Native x-space MPI image. Total acquisition time: 8 s ( $N = 2$  averaged frames). FOV: 10 cm  $\times$  5.0 cm.

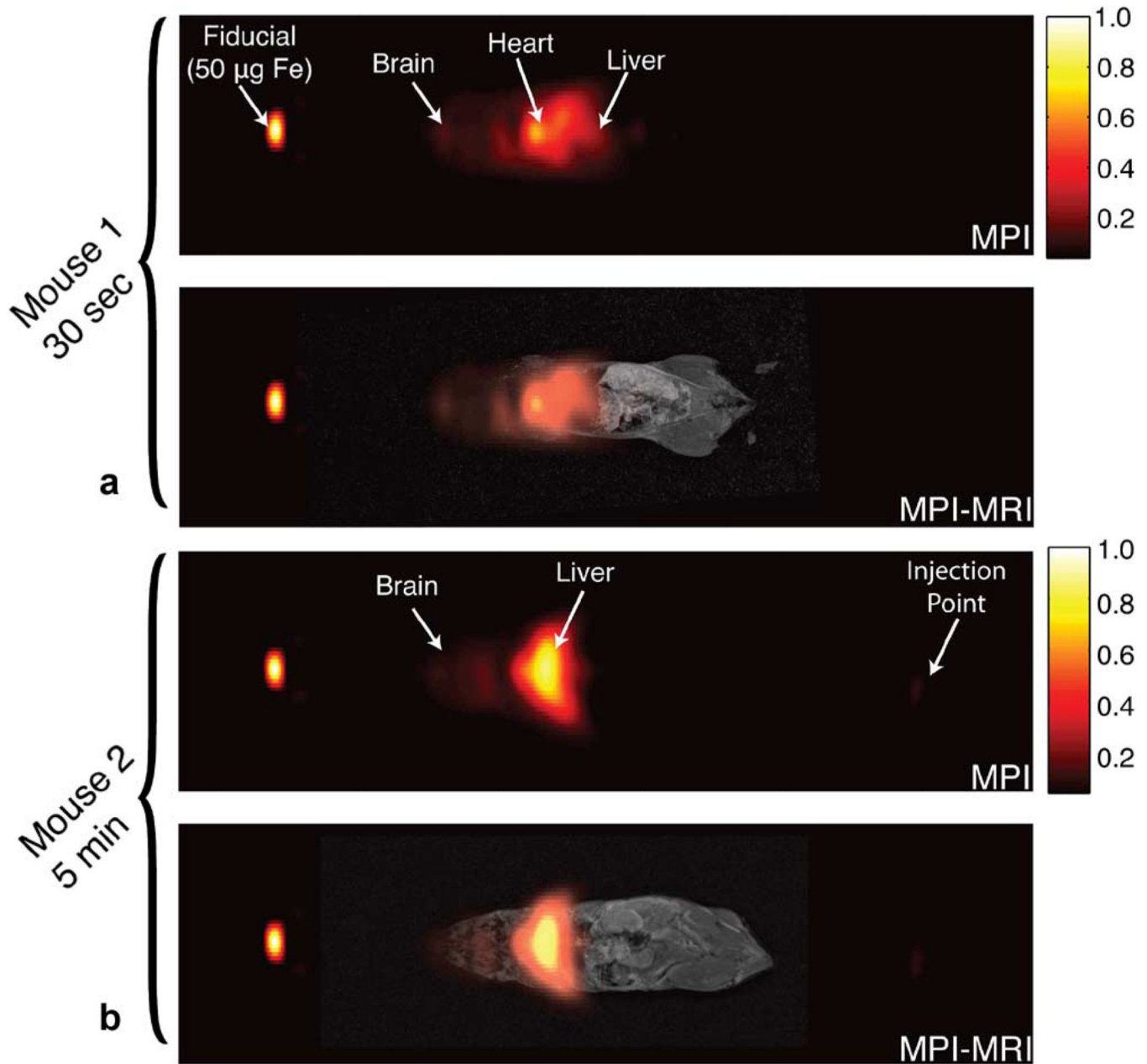


**Fig. 11.**

(a) Full-body MPI projection scan of a mouse injected in a tail vein with 20  $\mu\text{L}$  (556  $\mu\text{g}$  Fe) undiluted Resovist tracer and sacrificed after 30 s. The resulting MPI image shows a MPI-MRI visible fiducial (50  $\mu\text{g}$  Fe), as well as the outlines of the mouse brain, heart, and liver. (b) Full-body MPI projection scan of an identically prepared mouse, but with a pause of 5 min after injection and before sacrifice. In the projection MPI scan, it is apparent that the Resovist tracer is rapidly filtered from the blood stream by the liver. The MRI scan (taken post-sacrifice) shows a dark liver as Resovist is a  $T_2^*$  agent. Total scan time: 8 s. MPI FOV = 6 cm  $\times$  20 cm. Both images are scaled so that the 50  $\mu\text{g}$  fiducial has a signal intensity of 1.